materials

MDPI

Article

Effect of Chemical Composition on the Thermoplastic Formability and Nanoindentation of Ti-Based Bulk Metallic Glasses

Mengliang Chen [1], Liu Zhu [2,*], Yingwei Chen [3], Sheng Dai [2], Qijie Liu [3], Na Xue [2], Weiwei Li [2], Jinfang Wang [2], Yingqi Huang [2], Kaice Yang [2] and Ling Shao [2,*]

[1] School of Materials Science and Engineering, Zhejiang Sci-Tech University, Hangzhou 310018, China
[2] Zhejiang Provincial Key Laboratory for Cutting Tools, Taizhou University, Taizhou 318000, China; sdai@tzc.edu.cn (S.D.); xuena@tzc.edu.cn (N.X.); lww@tzc.edu.cn (W.L.); wjf0909@tzc.edu.cn (J.W.); yingqihuang77@hotmail.com (Y.H.); 17338523070@163.com (K.Y.)
[3] Taizhou Key Laboratory of Medical Devices and Advanced Materials, Research Institute of Zhejiang University-Taizhou, Taizhou 318000, China; cywsn@163.com (Y.C.); tanksman@163.com (Q.L.)
* Correspondence: zhuliu@tzc.edu.cn (L.Z.); lingshaocn@hotmail.com (L.S.)

Abstract: A series of $Ti_{41}Zr_{25}Be_{34-x}Ni_x$ (x = 4, 6, 8, 10 at.%) and $Ti_{41}Zr_{25}Be_{34-x}Cu_x$ (x = 4, 6, 8 at.%) bulk metallic glasses were investigated to examine the influence of Ni and Cu content on the viscosity, thermoplastic formability, and nanoindentation of Ti-based bulk metallic glasses. The results demonstrate that $Ti_{41}Zr_{25}Be_{30}Ni_4$ and $Ti_{41}Zr_{25}Be_{26}Cu_8$ amorphous alloys have superior thermoplastic formability among the $Ti_{41}Zr_{25}Be_{34-x}Ni_x$ and $Ti_{41}Zr_{25}Be_{34-x}Cu_x$ amorphous alloys due to their low viscosity in the supercooled liquid region and wider supercooled liquid region. The hardness and modulus exhibit obvious variations with increasing Ni and Cu content in Ti-based bulk metallic glasses, which can be attributed to alterations in atomic density. Optimal amounts of Ni and Cu in Ti-based bulk metallic glasses enhance thermoplastic formability and mechanical properties. The influence of Ni and Cu content on the hardness of Ti-based bulk metallic glasses is discussed from the perspective of the mean atomic distance.

Keywords: Ti-based bulk metallic glass; viscosity; thermoplastic formability; nanoindentation; average atomic distance

Citation: Chen, M.; Zhu, L.; Chen, Y.; Dai, S.; Liu, Q.; Xue, N.; Li, W.; Wang, J.; Huang, Y.; Yang, K.; et al. Effect of Chemical Composition on the Thermoplastic Formability and Nanoindentation of Ti-Based Bulk Metallic Glasses. *Materials* **2024**, *17*, 1699. https://doi.org/10.3390/ma17071699

Academic Editor: Mihai Stoica

Received: 19 February 2024
Revised: 2 April 2024
Accepted: 5 April 2024
Published: 8 April 2024

1. Introduction

Bulk metallic glasses (BMGs) exhibit remarkable mechanical properties and superb corrosion resistance due to their microstructure of short-range order and long-range disordered atomic arrangement [1–5]. As a result, BMGs have tremendous potential as structural materials in aerospace, electronic devices, medical equipment, and other fields [6–8]. Among the various types of existing BMGs, Ti-based BMGs have been paid widespread attention owing to their high specific strength, good corrosion resistance, light weight, biocompatibility, and low cost [9–12]. Ti-based BMGs can be used to manufacture solar wind collectors for absorbing and retaining higher-energy ions [13]. Ti-based BMGs have been applied in preparing Coriolis flow meter sensing tubes, which can be used in chemical industry and semiconductor fields [14]. Additionally, the exceptional mechanical strength of Ti-based BMGs endows them with remarkable load-bearing capacity, an elasticity modulus resembling that of human bone structure, and favorable biocompatibility. These inherent advantages position Ti-based BMG as highly promising materials in the field of biomedical engineering for applications such as medical devices or implants. Liens et al. [15] conducted a comprehensive and exhaustive characterization of $Ti_{40}Zr_{10}Cu_{36}Pd_{14}$ BMG, which was deemed suitable for the fabrication of implants and abutment assemblies or small dimensional pieces for potential dental applications in the future.

However, the critical casting diameter of BMGs used to describe their glass forming abilities (GFAs) seriously limits their practical application [16]. Alloying is an effective method to improve the GFAs of BMGs. Currently, numerous Ti-based BMGs have been developed, including Ti-(Cu, Be) systems [17,18], Ti-Cu-(Ni, Co,) systems [19,20], Ti-Zr-(Cu, Be) systems [17,21], Ti-Zr-Cu-Ni-Be systems [22], and the like. Typical ternary Ti-Zr-Be BMGs with good GFAs can reach the critical diameter of 5 mm [23]. Based on this, Zhao et al. [24–26] and Gong et al. [27,28] prepared a series of Ti-Zr-Be-(Ag, Ni, Co, Cu, Fe) quaternary BMGs with good GFAs via an alloying method, of which the maximum critical diameter reached 20 mm. Tang et al. [29] reported a series of $(Ti_{36.1}Zr_{33.2}Ni_{5.8}Be_{24.9})_{100-x}Cu_x$ BMGs, with the maximum attainable diameter exceeding 50 mm and reaching up to 60 mm. Zhang et al. [30] investigated Ti-Zr-Cu-Fe-Be BMGs, which can achieve a max diameter of up to 50 mm. In addition, in order to avoid toxic metals, biocompatible Ti–Zr–Ta–Si and Ti–Zr–Pd–Si BMGs were manufactured by Oak et al. [31]. These works greatly promoted the application and development of quaternary Ti-based BMGs.

On the other hand, most BMGs have high hardness but lack room temperature plasticity, resulting in catastrophic failure under external loading, making cold work and machining very difficult [32]. The exceptional superplasticity exhibited by BMGs within the supercooled liquid region (SCLR) renders them ideal materials for precise net shaping of various geometries via thermoplastic forming (TPF), overcoming the inherent limitations associated with poor processability of BMGs at ambient temperatures [33]. The TPF of BMGs in the SCLR is controlled by temperature-dependent viscosity and temperature-dependent crystalline [34]. The viscosity of BMGs gradually decreases by several orders of magnitude with increasing temperature in the SCLR, and the processing accuracy can reach the nanometer scale with TPF technology, making BMGs the ideal material for microdevices [32,35]. Gong et al. [36] successfully fabricated $Ti_{41}Zr_{25}Be_{30}Fe_5$ nanorods via TPF. Cai et al. [37] successfully developed a 300 μm square-well array pattern and a 5 μm square-hump array on the surface of $Ti_{40}Zr_{10}Cu_{34}Pd_{14}Sn_2$ using TPF, showcasing the potential for intricate patterning. Additionally, Cai et al. [38] extended this work by fabricating a hierarchical structure on the surface of $Ti_{40}Zr_{10}Cu_{34}Pd_{14}Sn_2$ BMG through a two-step TPF process, effectively creating 400 nm protrusions atop 2.5 μm square humps. This marked the first instance of a Ti-based BMG achieving a layered structure with both micro-patterns and nano-patterns on the same surface. They further investigated the influence of various TPF conditions on the structural and mechanical properties of $Ti_{40}Zr_{10}Cu_{34}Pd_{14}Sn_2$ BMG, as well as its compatibility with cellular environments.

However, research on the TPF of Ti-based BMGs is currently limited. To enhance the TPF of BMGs, methods such as incorporating a wetting layer can be employed [39]. Additionally, adjusting the chemical composition of BMGs remains the most effective approach to improve their TPF. Obvious differences of TPF have been observed in different BMGs [34]. At present, there is limited research available on the composition-dependent TPF of Ti-based BMGs. However, TPF requires that the BMGs possess a sufficiently high GFA, as TPF only can be performed after obtaining the BMGs [40]. Therefore, the effect of chemical composition on the TPF of quaternary Ti-based BMGs with high GFA was investigated, which is significant for promoting the application of Ti-based BMGs. In this study, $Ti_{41}Zr_{25}Be_{34-x}Ni_x$ (at.%) and $Ti_{41}Zr_{25}Be_{34-x}Cu_x$ (at.%) BMG systems were employed to investigate the effect of the change of Ni and Cu content on the thermal stability, TPF, viscosity, and nanoindentation. The correlation between mean atomic distance and hardness is also discussed for $Ti_{41}Zr_{25}Be_{34-x}Ni_x$ (at.%) and $Ti_{41}Zr_{25}Be_{34-x}Cu_x$ (at.%) BMG systems.

2. Experimental Materials and Methods

The master ingots with normal compositions of $Ti_{41}Zr_{25}Be_{34-x}Ni_x$ (hereafter, x = 4, 6, 8, 10 are denoted as Ni4, Ni6, Ni8, and Ni10, respectively) and $Ti_{41}Zr_{25}Be_{34-x}Cu_x$ (hereafter, x = 4, 6, and 8 are denoted as Cu4, Cu6, and Cu8, respectively) were fabricated using a KDH-300 induction melting furnace (Henan Kusite Instrument Technology Co., Ltd.,

Zhengzhou, Henan, China) by arc-melting a blend of high-purity metals (purity ≥ 99.99%) in a Ti-gettered high-purity argon atmosphere. The pure titanium ingot was melted prior to melting the master ingot in order to effectively absorb any residual oxygen. The master ingot, weighing approximately 10 g, was flipped and remelted four times to ensure compositional homogeneity. Cylindrical rods with a 6 mm diameter and a 50 mm length were prepared via a copper mold suction casting method. The amorphous structure of the as-cast samples was checked using a Bruker D8 Advance X-ray diffractometer (Rigaku Industrial Co., Ltd., Tokyo, Japan) with Cu Kα radiation in the 2θ range of 10–90° at a 0.02° scanning step and a 3° min^{-1} scanning speed. Differential scanning calorimetry (DSC) tests were performed by a Netzsch STA 449 F3 (NETZSCH-Gerätebau GmbH, Selb, Wunsiedel, Germany) under a flow of purified argon at a 20 K min^{-1} heating rate, using alumina crucibles.

A simple and precise standard, the maximum strain a BMG can undergo in its supercooled liquid state before it eventually crystallizes, was used to characterize the TPF of BMG [34]. The TPF of $Ti_{41}Zr_{25}Be_{34-x}Ni_x$ and $Ti_{41}Zr_{25}Be_{34-x}Cu_x$ BMG systems characterized by the final diameter D was tested according to the standard. Before testing, the top and bottom surfaces of the Ti-based BMG samples were ground using 2000 grit sandpapers. The BMG specimens were positioned between platens and forced against each other with a constant load of 2000 N, using an OTF-1200X-VHP4 hot-pressing machine (Hefei Kejing Material Technology Co., Ltd., Hefei, Anhui, China). The sample volume was about 0.1 cm^3, the starting processing temperature was glass transition temperature T_g, the constant heating rate was 1 K min^{-1}, and the highest processing temperature was chosen as that at which crystallization can still be avoided, in order to maximize the formability during TPF process [41]. The viscosity η of the amorphous alloys in SCLR is a very important parameter, which determines the processing formability [42]. The viscosity of the samples was determined through thermomechanical analyzer (TMA) analysis to further examine the influence of chemical composition on the TPF of Ti-based BMGs. The geometric dimension of viscosity samples was Φ6 mm × 5 mm. The viscosity tests were performed as a function of temperature in the SCLR using TA Q400 TMA (TA Instruments Inc., Wilmington City, DE, USA) with a 10 K min^{-1} heating rate and a 1 N static force. The η of BMGs was determined according to the following equation, as given in [43,44]:

$$\eta = \frac{\sigma_{\text{flow}}}{3\dot{\varepsilon}} \quad (1)$$

where $\dot{\varepsilon}$ denotes the strain rate of the BMGs and σ_{flow} is the flow stress of the BMGs. In order to study the relationship between chemical composition and nanoindentation, porosities that remained in the as-cast specimens were excluded to prepare nanoindentation samples via TPF in the SCLR. To control their fictive temperature, all alloys were cooled after TPF from a temperature of ~T_g + 20 K through the glass transition region at a rate of ~50 K s^{-1}.

Prior to conducting the nanoindentation tests, special attention was given to the surface quality of the samples. The samples were ground using 400, 800, 1500, and 2500 grit sequentially, followed by a final polishing step with an alumina paste to achieve a mirror-like finish, and no discernible scratches were observed. Nanoindentation tests were carried out using a U9820A Nano Indenter G200 (Agilent Technologies Inc., Santa Clara City, CA, USA) under the load control mode with a 40 mN peak load for 5 s. Both the loading and unloading rates were set as 1 mN s^{-1}. For each sample, the indentation process was repeated five times with the indents spaced 100 μm apart.

3. Results

3.1. Amorphous Nature

The X-ray diffraction (XRD) patterns of the as-cast materials show that the expected broad amorphous halos with no crystallization were observed (Figure 1a,c). Clear glass transitions and sharp crystallization events were observed in the DSC thermograms (Figure 1b,d), where the T_g and onset temperature of crystallization T_x can be identified, confirming the glassy

nature of $Ti_{41}Zr_{25}Be_{34-x}Ni_x$ and $Ti_{41}Zr_{25}Be_{34-x}Cu_x$ BMGs. The width of SCLR, defined as $\Delta T = T_x - T_g$, has often been used to evaluate the thermostability of SCLR [45]. The thermal parameters of $Ti_{41}Zr_{25}Be_{34-x}Ni_x$ and $Ti_{41}Z_{r25}Be_{34-x}Cu_x$ BMGs are summarized in Table 1. The T_g decreased from 601 K at Ni4 BMG to 591 K at Ni8 BMG, followed by a slight increase to 595 K at Ni10 BMG. The T_g of $Ti_{41}Zr_{25}Be_{34-x}Cu_x$ BMGs exhibited a decrease followed by a subsequent increase with Cu content. The change trend of T_g of the $Ti_{41}Zr_{25}Be_{34-x}Ni_x$ and $Ti_{41}Zr_{25}Be_{34-x}Cu_x$ BMG systems is in good agreement with the data of other researchers [19,22]. The reduced glass transition temperature, T_{rg} ($=T_g/T_l$) [46], has been often quoted to evaluate the GFA of amorphous materials [47]. From Table 1, it can be seen that for the $Ti_{41}Zr_{25}Be_{34-x}Ni_x$ alloy series, T_{rg} monotonically increased with increasing Ni content from 0.5380 for Ni4 BMG to 0.5716 for Ni10 BMG. For the $Ti_{41}Zr_{25}Be_{34-x}Cu_x$ alloy series, T_{rg} also monotonically increased with increasing Cu content from 0.5169 for Cu4 BMG to 0.5288 for Cu8 BMG. ΔH_m represents the crystallization enthalpy and was calculated from the DSC curves (Figure 1b,d). In the Ti-Zr-Be-Ni BMG system, the ΔH_m decreased from -22.29 J g^{-1} at Ni4 BMG to -34.37 J g^{-1} at Ni6 BMG, followed by increasing to -26.23 J g^{-1} at Ni10 BMG. The ΔH_m of Cu4, Cu6, and Cu8 BMGs was -25.95 J g^{-1}, -35.22 J g^{-1} and -27.00 J g^{-1}, respectively.

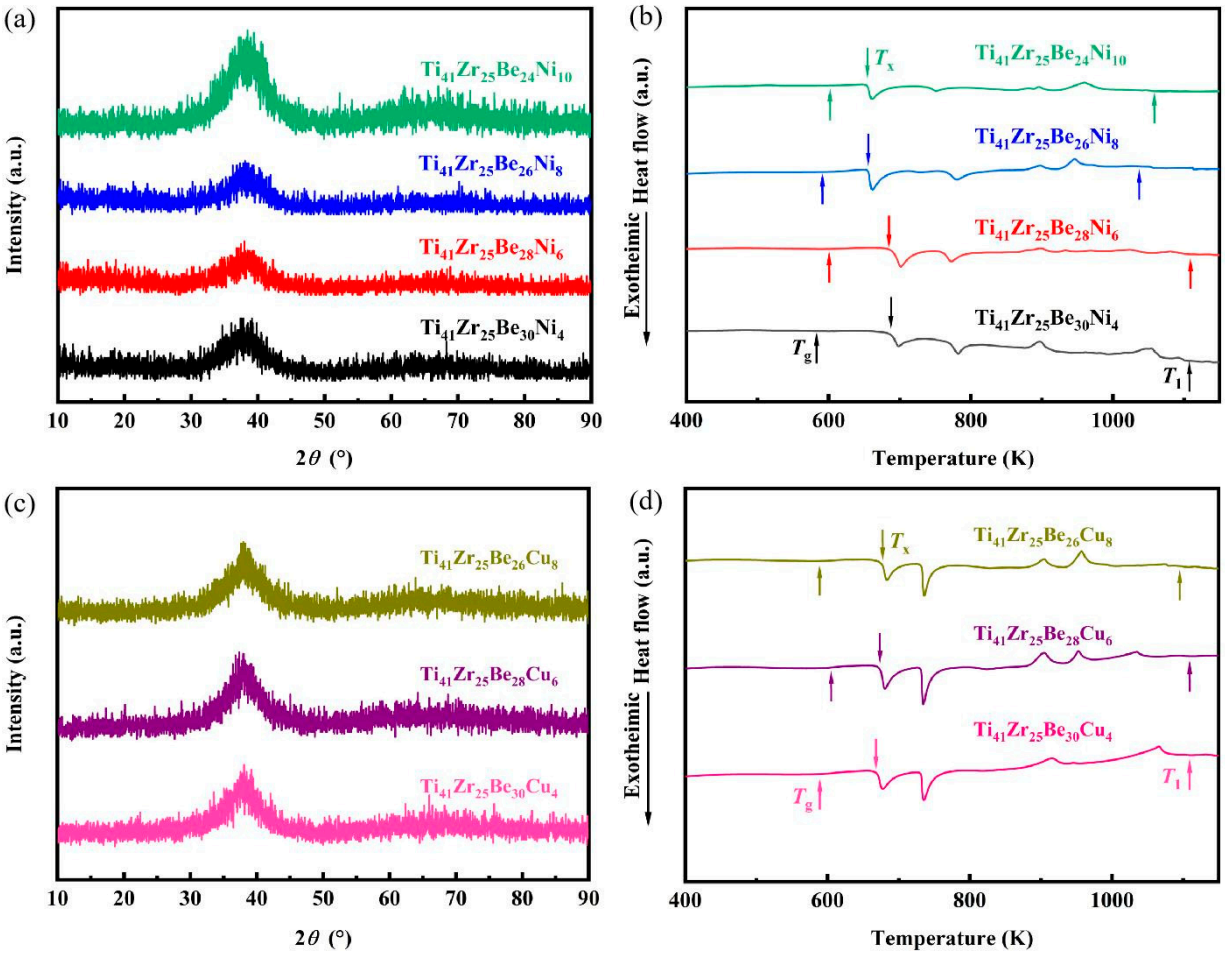

Figure 1. Structure and thermal characterization of $Ti_{41}Zr_{25}Be_{30-x}Ni_x$ and $Ti_{41}Zr_{25}Be_{30-x}Cu_x$ BMG systems. (**a**) XRD patterns of the $Ti_{41}Zr_{25}Be_{34-x}Ni_x$ BMGs with 6 mm rods. *θ:* XRD scattering angle; a.u.: arbitrary unit. (**b**) DSC curves of $Ti_{41}Zr_{25}Be_{30-x}Ni_x$ alloys (the heating rate is 20 K min^{-1}). (**c**) XRD patterns of the $Ti_{41}Zr_{25}Be_{30-x}Cu_x$ BMGs with 6 mm rods. (**d**) DSC curves of $Ti_{41}Zr_{25}Be_{34-x}Cu_x$ alloys.

Table 1. Glass transition temperature (T_g), onset temperature of crystallization (T_x), crystallization exothermic heat (ΔH), melting temperature (T_m), and liquid temperature (T_l) of $Ti_{41}Zr_{25}Be_{30-x}Ni_x$ and $Ti_{41}Zr_{25}Be_{34-x}Cu_x$ BMGs obtained via DSC at a heating rate of 20 K min^{-1}, $\Delta T_x = T_x - T_g$, $T_{rg} = T_g/T_l$, $S = \Delta T_x/(T_l - T_g)$.

Composition	T_g (K)	T_x (K)	ΔT_x (K)	T_m (K)	T_l (K)	T_{rg}	ΔH_m (J g^{-1})	S
$Ti_{41}Zr_{25}Be_{30}Ni_4$	601	684	83	876	1118	0.5380	−22.29	0.1605
$Ti_{41}Zr_{25}Be_{28}Ni_6$	597	680	83	868	1108	0.5388	−34.37	0.1624
$Ti_{41}Zr_{25}Be_{26}Ni_8$	591	655	64	874	1050	0.5629	−33.23	0.1394
$Ti_{41}Zr_{25}Be_{24}Ni_{10}$	595	654	59	864	1041	0.5716	−26.23	0.1323
$Ti_{41}Zr_{25}Be_{30}Cu_4$	579	669	90	870	1120	0.5169	−25.95	0.1664
$Ti_{41}Zr_{25}Be_{28}Cu_6$	590	674	84	881	1119	0.5273	−35.22	0.1588
$Ti_{41}Zr_{25}Be_{26}Cu_8$	578	673	95	885	1093	0.5288	−27.00	0.1845

3.2. Thermoplastic Formability

The TPF of $Ti_{41}Zr_{25}Be_{34-x}Ni_x$ and $Ti_{41}Zr_{25}Be_{34-x}Cu_x$ BMG series exhibited significant variation depending on the chemical composition (presented in Figure 2). The TPF of Ni4 BMG was the best among $Ti_{41}Zr_{25}Be_{34-x}Ni_x$ amorphous alloys and the TPF of Cu8 BMG was the best among $Ti_{41}Zr_{25}Be_{34-x}Cu_x$ amorphous alloys. The D of the $Ti_{41}Zr_{25}Be_{34-x}Ni_x$ alloy system decreased from Ni4 at D = 9.73 mm to D = 6.42 mm at Ni10; however, the D of the $Ti_{41}Zr_{25}Be_{34-x}Cu_x$ alloy system increased from Cu4 at D = 7.78 mm to D = 10.04 mm at Cu8. This indicates that the TPF of $Ti_{41}Zr_{25}Be_{34-x}Ni_x$ BMGs decreases with the increase in Ni content; however, the TPF of $Ti_{41}Zr_{25}Be_{34-x}Cu_x$ BMGs increases with increasing Cu content. Generally, the width of the SCLR is one of the important indicators of TPF. A wider SCLR not only means better thermal stability of BMGs, but can also better avoid the crystallization of BMGs in the TPF process. Therefore, $S = \Delta T_x/(T_l - T_g)$ was presented as a strong indicator of correlation with TPF [27,48,49]. In this sense, a higher value of S is indicative of the TPF of the investigated Ti-based BMGs to a certain extent. As illustrated in Table 1, the Cu8 alloy possessed a larger S value of 0.1844 compared with other studied Ti-Zr-Be-(Ni, Cu) BMGs, and its D value (10.04 mm) also ranked highest among the Ti-Zr-Be-(Ni, Cu) BMGs.

3.3. Viscosity

The TMA results of the investigated $Ti_{41}Zr_{25}Be_{34-x}Ni_x$ and $Ti_{41}Zr_{25}Be_{34-x}Cu_x$ BMG series are presented in Figure 3. The TMA curves exhibit a decrease in compressive deformation (Δh) with increasing Ni content in the $Ti_{41}Zr_{25}Be_{34-x}Ni_x$ BMG system (Figure 3a), while an increase in Δh can be observed with the increase in Cu content in the $Ti_{41}Zr_{25}Be_{34-x}Cu_x$ BMG system (Figure 3c). $Ti_{41}Zr_{25}Be_{30}Ni_4$ BMG presents the largest Δh with 174.0 um and $Ti_{41}Zr_{25}Be_{26}Cu_8$ BMG exhibits the largest Δh with 153.3 um. The value of Δh also indicates the TPF of the BMG samples in the SCLR. For example, Pan Gong et al. [27] used Δh to characterize the TPF of Ti-Zr-Be-Co BMGs. In order to investigate the influence of key parameters on the TPF, the TMA results were converted into a plot of viscosity versus temperature via Equation (1). The variation of viscosity with temperature in the SCLR for $Ti_{41}Zr_{25}Be_{34-x}Ni_x$ and $Ti_{41}Zr_{25}Be_{34-x}Cu_x$ BMGs is depicted in Figure 3b and 3d, respectively. The viscosity of $Ti_{41}Zr_{25}Be_{34-x}Ni_x$ and $Ti_{41}Zr_{25}Be_{34-x}Cu_x$ BMGs exhibits a significant variation with a pronounced decrease by several orders of magnitude at the T_g temperature and an increase as it approaches the T_x temperature.

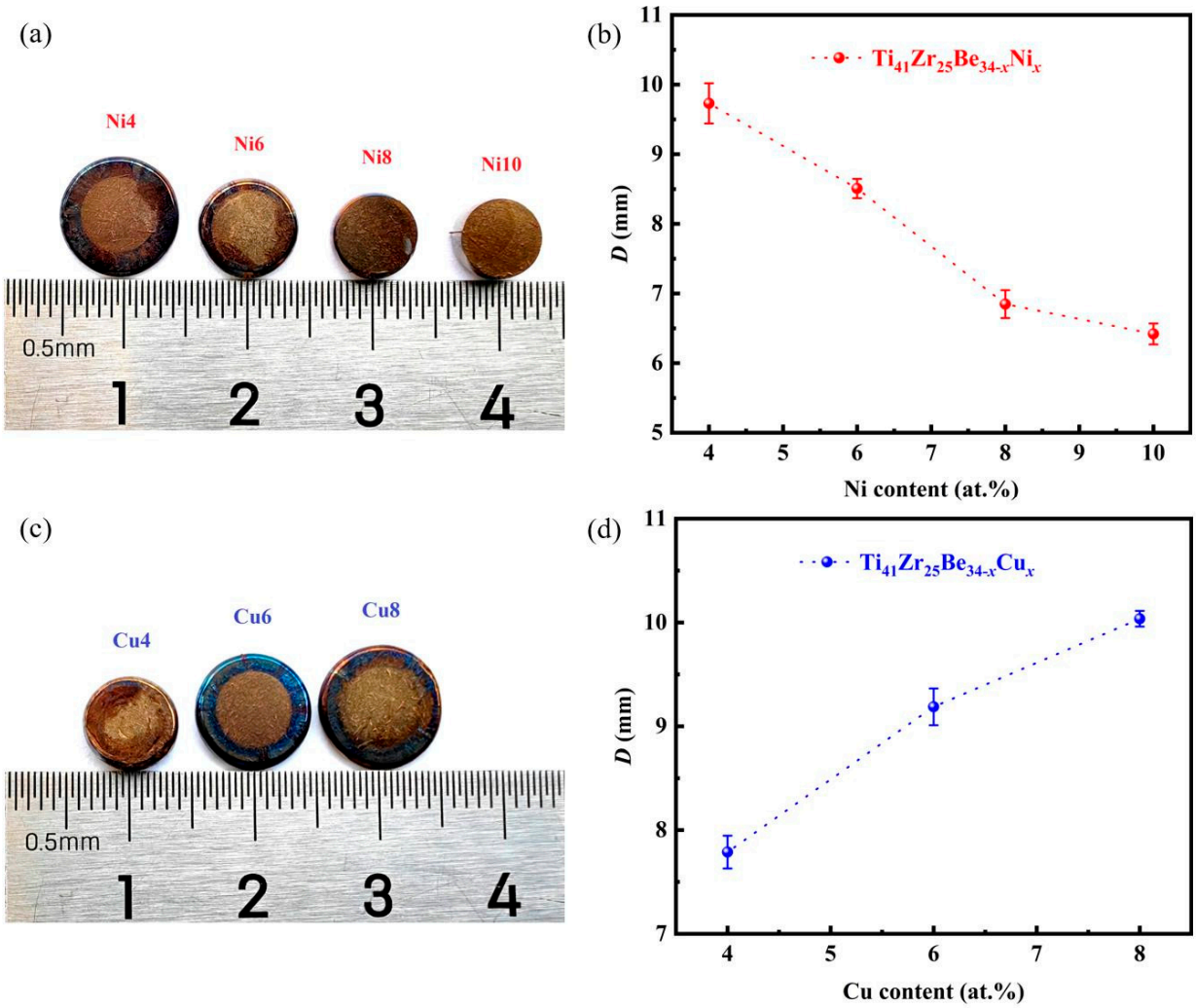

Figure 2. Thermoplastic formability of $Ti_{41}Zr_{25}Be_{34-x}Ni_x$ and $Ti_{41}Zr_{25}Be_{34-x}Cu_x$ BMG series. (**a**) Top view of the $Ti_{41}Zr_{25}Be_{34-x}Ni_x$ samples after the thermoplastic formability characterization evaluation. (**b**) Change of *D* as a function of the Ni content. (**c**) Top view of the $Ti_{41}Zr_{25}Be_{34-x}Cu_x$ samples after the thermoplastic formability characterization evaluation. (**d**) Change of *D* as a function of the Cu content.

The viscosity includes secondary drops (indicated by the arrow), which can be observed in the Ni4, Cu6, and Cu8 alloys. This phenomenon was also observed by Parthiban et al. [50] and Stoica et al. [51], who reported that the investigated Fe-Co-B-Si-Nb-Cu BMGs presented two glass-transition-like events. The above case may indicate that after the initial crystallization, the samples exhibit a structure comprising a crystalline phase along with the remaining amorphous matrix.

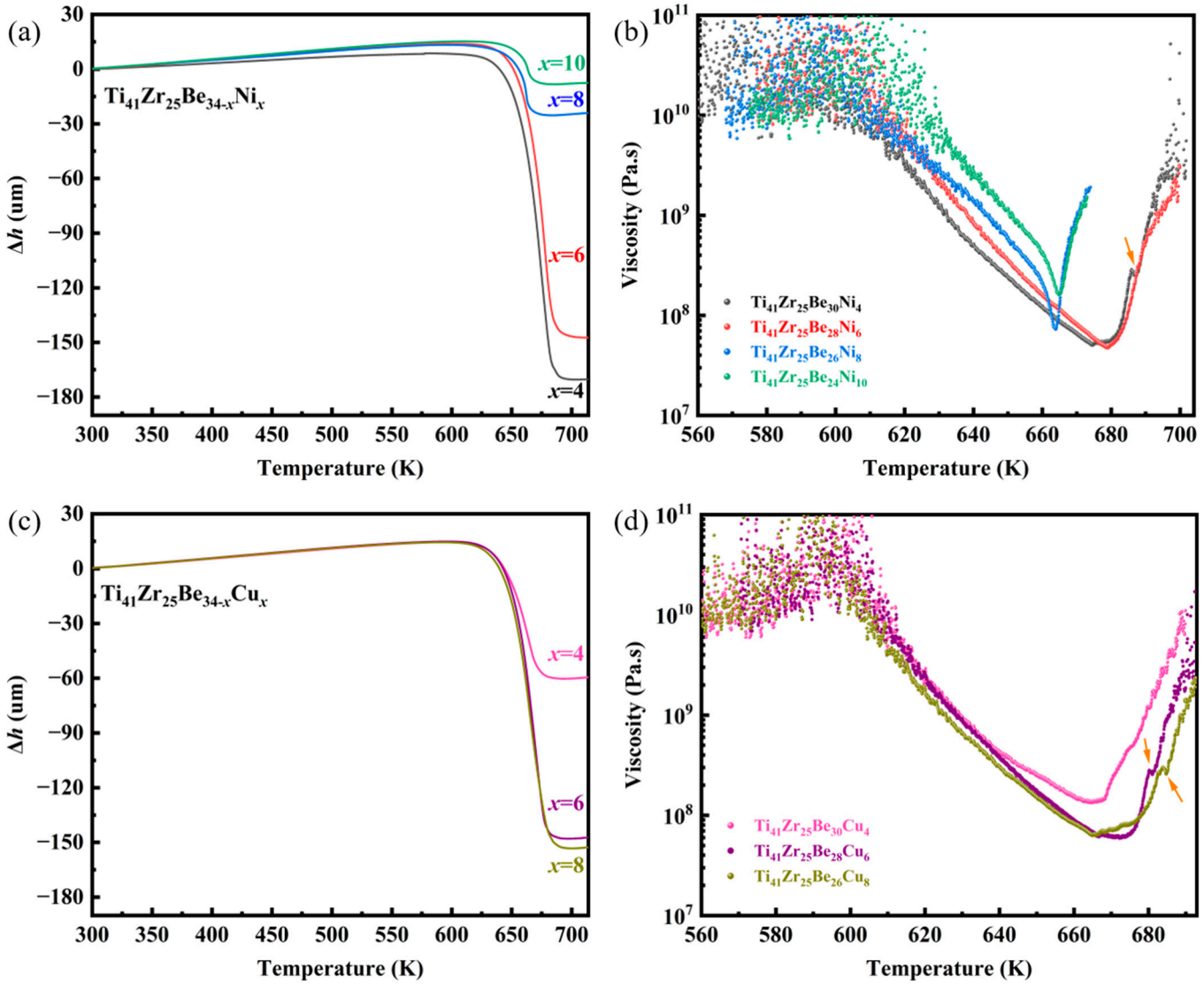

Figure 3. Viscosity as a function of temperature of the Ti-based BMGs. (**a**) TMA curves of $Ti_{41}Zr_{25}Be_{34-x}Ni_x$. (**b**) Measured viscosity of the $Ti_{41}Zr_{25}Be_{34-x}Ni_x$ BMGs in the SCLR. (**c**) TMA curves of $Ti_{41}Zr_{25}Be_{34-x}Cu_x$. (**d**) Measured viscosity of the $Ti_{41}Zr_{25}Be_{34-x}Cu_x$ BMGs in the SCLR.

3.4. Nanoindentations

The typical load–displacement (*P-h*) curves of $Ti_{41}Zr_{25}Be_{34-x}Ni_x$ and $Ti_{41}Zr_{25}Be_{34-x}Cu_x$ BMG systems are given in Figures 4a and 5a, respectively. To obtain a comprehensive analysis of the loading part, each *P-h* curve has been horizontally shifted by some distance to the right, and the *P-h* curves present the same change trend. The rectangular dotted zone in Figure 4a is magnified to provide a close-up view of the *P-h* curves of $Ti_{41}Zr_{25}Be_{34-x}Ni_x$ BMGs, as shown in Figure 4c–f, and the rectangular dotted zone in Figure 5a is also magnified to provide a close-up view of the *P-h* curves of $Ti_{41}Zr_{25}Be_{34-x}Cu_x$ BMGs, as shown in Figure 5c–e. For $Ti_{41}Zr_{25}Be_{34-x}Ni_x$ and $Ti_{41}Zr_{25}Be_{34-x}Cu_x$ BMG systems, the serrated flows and platforms in the *P-h* curves are observed in the magnified zones of the *P-h* curves. The platform continues to deform even after reaching maximum load, indicating the occurrence of creep as the indentation depth further increases under maximum load [52]. Subsequently, during unloading, elastic recovery is observed with a decrease in indentation depth. The occurrence of serrated flows in the loading curves is attributed to the propagation of shear bands [53]. The nanoindentation tests induced both plastic and elastic deformation in the

samples. The occurrence of serrated flows is associated with localized plastic flow of BMGs, indicating the activation of shear bands [54,55].

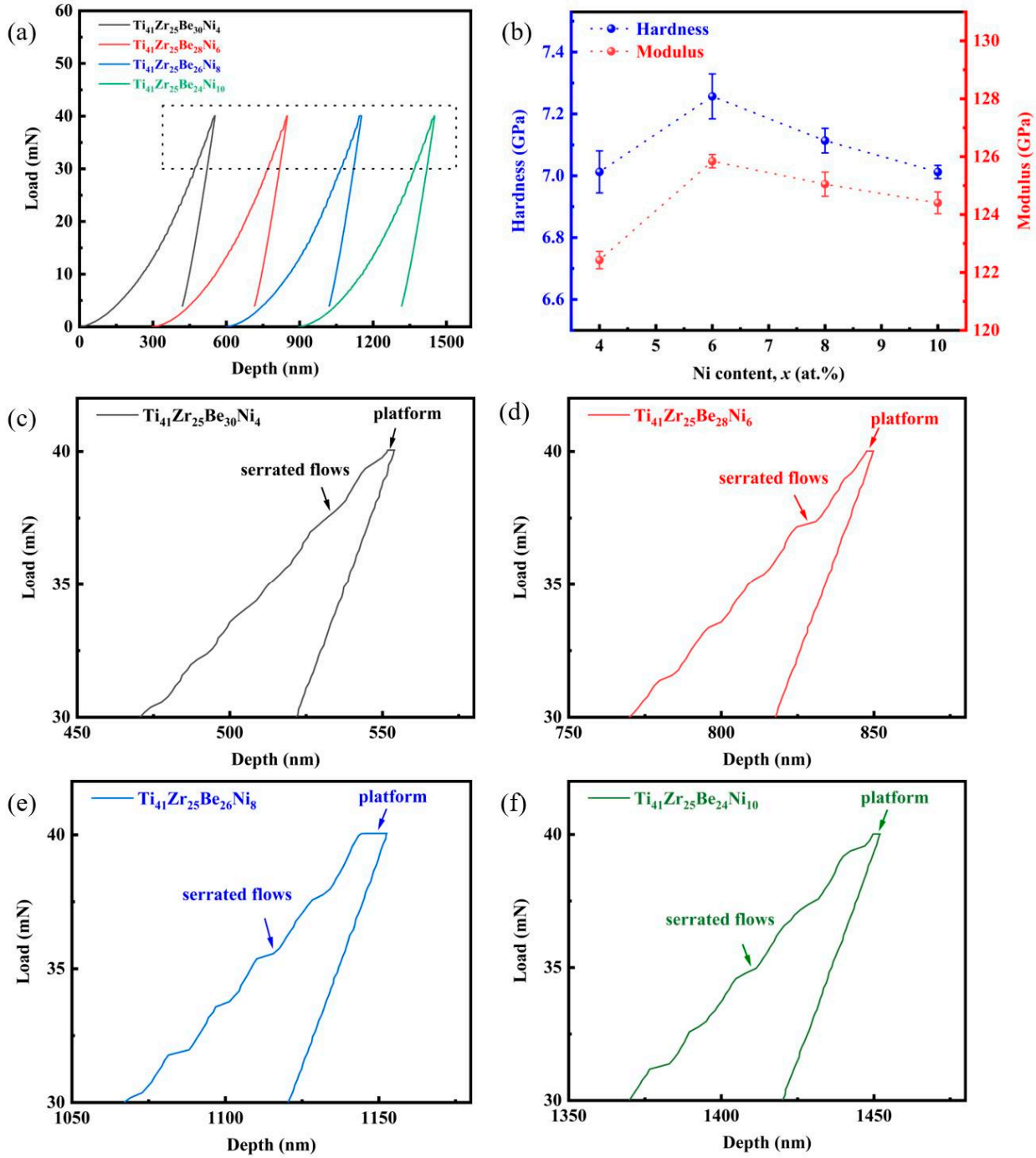

Figure 4. Nanoindentation results of $Ti_{41}Zr_{25}Be_{34-x}Ni_x$ BMG system. (**a**) Representative *P-h* curves of $Ti_{41}Zr_{25}Be_{34-x}Ni_x$ BMGs at a constant loading rate of 1 mN s^{-1}; (**b**) relationship between hardness, modulus, and Ni content; (**c**–**f**) a close view of the rectangular dotted zone in Figure 4a.

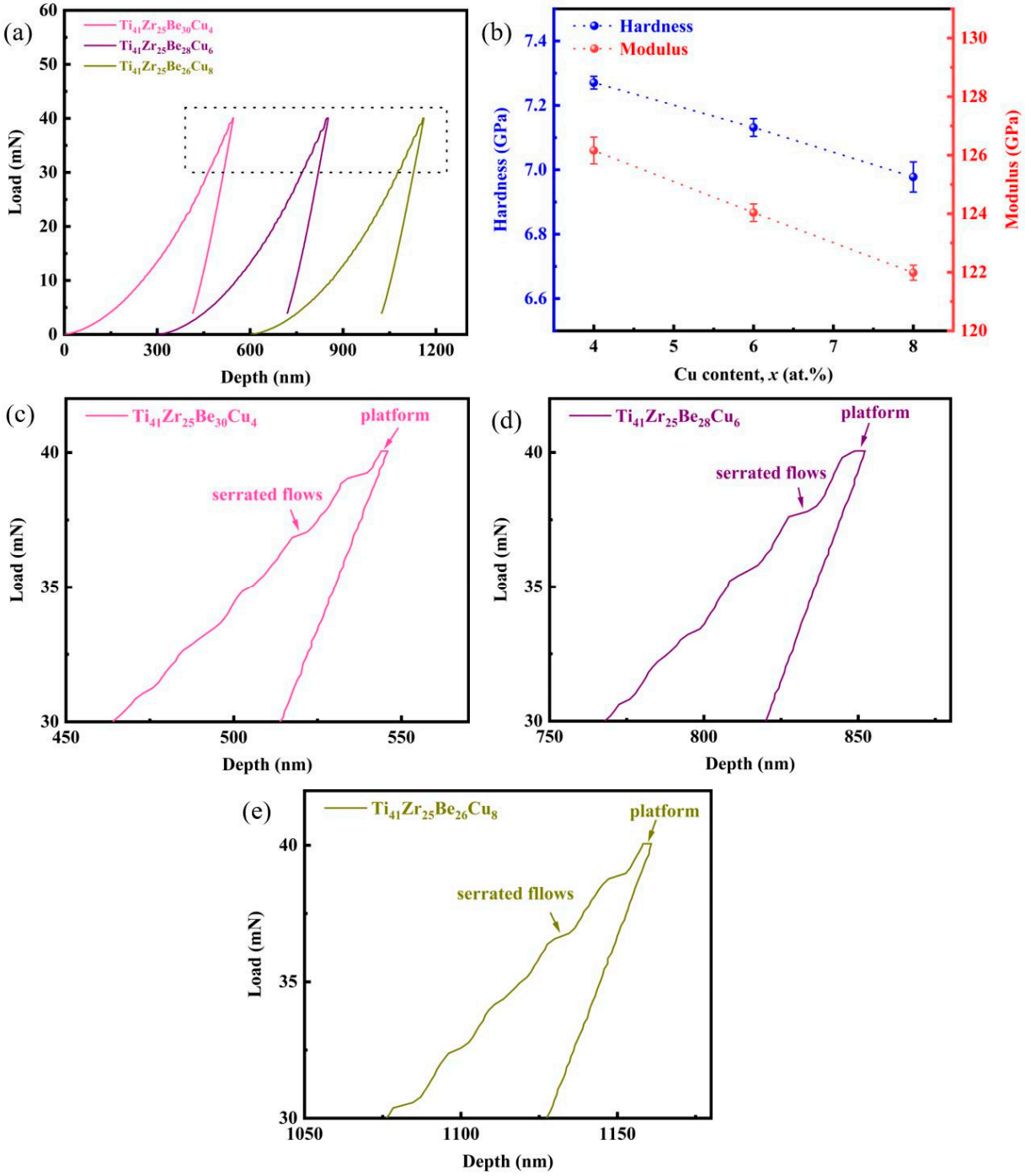

Figure 5. Nanoindentation results of $Ti_{41}Zr_{25}Be_{34-x}Cu_x$ BMG system. (**a**) Representative *P-h* curves of $Ti_{41}Zr_{25}Be_{34-x}Cu_x$ BMGs at a constant loading rate of 1 mN s^{-1}; (**b**) relationship between hardness, modulus, and Cu content; (**c**–**e**) a close view of the rectangular dotted zone in Figure 5a.

The results for the hardness (*H*) and elastic modulus (*E*) of $Ti_{41}Zr_{25}Be_{34-x}Ni_x$ and $Ti_{41}Zr_{25}Be_{34-x}Cu_x$ BMG series calculated using the Oliver–Pharr method [56] are shown in Figures 4b and 5b, respectively. The *H* of $Ti_{41}Zr_{25}Be_{34-x}Ni_x$ BMGs first increased from Ni4 BMG with *H* = 7.01 GPa to *H* = 7.26 GPa at Ni6 BMG, and then decreased with further increasing Ni content to *H* = 7.03 GPa for Ni10 BMG. The *E* of $Ti_{41}Zr_{25}Be_{34-x}Ni_x$ BMGs initially increased with Ni content and reached a maximum of *H* = 125.84 GPa at Ni6 BMG, and then decreased with increasing Ni content. The change trend of *E* for the

$Ti_{41}Zr_{25}Be_{34-x}Ni_x$ BMGs is the same as that of H for $Ti_{41}Zr_{25}Be_{34-x}Ni_x$ BMGs, while both the H and E of $Ti_{41}Zr_{25}Be_{34-x}Cu_x$ BMGs decreased with an increase in Cu content (Figure 5b).

4. Discussion

Enlarging the maximal diffracted intensity in Figure 1a,c, it can be observed that the angle at maximal diffracted intensity θ_m of $Ti_{41}Zr_{25}Be_{34-x}Ni_x$ BMGs first increased with the increase in Ni content, reached a peak at Ni6 BMG, and then decreased with an increase in Ni content (Figure 6a). The θ_m of $Ti_{41}Zr_{25}Be_{34-x}Cu_x$ BMGs decreased with increasing Cu content (Figure 6b). The position of θ_m was determined through simulation using the Gaussian model. Even though no quantitative analysis of the average atomic distance was tried, the model for diatomic gas introduced by Guinier [57] was utilized to monitor the alterations in the relative atomic structure of the studied alloys as their chemical composition changed. Hufnagel et al. [58], Caron et al. [59], Supriya et al. [60], Yang et al. [61], Sharma et al. [62], and Lv et al. [63] also applied this model to study the atomic structural changes in BMGs subjected to elastic stress and established a connection between the atomic distance of a diatomic gas molecule and the Bragg diffraction angle, via the following equation:

$$1.23\lambda = 2d\sin\theta \quad (2)$$

where λ is the wavelength of the radiation and d denotes the atomic distance of a diatomic gas. In Equation (2), the factor 1.23 is a result of the random orientation of molecules within the gas [57,62]. Initially, as a simplification, we can assume a similar relationship for the average atomic distance within an amorphous solid, replacing 1.23 with a factor K. Then, we can make the preliminary assumption that K remains constant over the entire concentration range under investigation and thus assess the relative alteration of the average atomic distance with a change in chemical composition.

The θ_m of $Ti_{41}Zr_{25}Be_{34-x}Ni_x$ alloys initially exhibited a slight increase and subsequently decreased with increasing Ni content (Figure 6c), resulting in a decrease followed by an increase in the value of d/K with increasing Ni content (Figure 6e). This implies that the mean atomic distance first decreased and then increased with increasing Ni content, and also indicates that then atomic density underwent an initial rise followed by a subsequent decline. The mass density increased from 5.07 g/cm^3 at Ni4 BMG to 5.138 g/cm^3 at Ni6 BMG, followed by a slight decrease to 5.072 g/cm^3 at Ni10 BMG. The mass density of the samples prepared for nanoindentation tests was determined using Archimedes' principle. In the $Ti_{41}Zr_{25}Be_{34-x}Ni_x$ BMG system, the mean atomic distance exhibited an inverse relationship with mass density. As a result, hardness initially increased and then further decreased with increasing Ni content (Figure 4b). When the Ni content was at 6 at.% in the $Ti_{41}Zr_{25}Be_{34-x}Ni_x$ BMG system, the d/K value reached its minimum, indicating that Ni6 possessed a more densely packed atomic structure and consequently exhibited the highest hardness (7.26 GPa). Following the same underlying principle, the θ_m decreased with an increase in Cu content in the $Ti_{41}Zr_{25}Be_{34-x}Cu_x$ alloys (Figure 6d), leading to an increase in d/K with increasing Cu content (Figure 6f). Figure 6f also illustrates that, in the as-cast state, the mean atomic distance of $Ti_{41}Zr_{25}Be_{34-x}Cu_x$ BMGs tended to increase as the Cu content increased, accordingly resulting in a decrease in atomic density. The mass density of $Ti_{41}Zr_{25}Be_{34-x}Cu_x$ BMGs exhibited a gradual decrease from 5.04 g/cm^3 at Cu4 BMG to 5.02 g/cm^3 at Cu8 BMG. In the $Ti_{41}Zr_{25}Be_{34-x}Cu_x$ BMG system, the mean atomic distance also exhibited an inverse relationship with mass density. Thus, the hardness decreased with an increase in Cu content. At 4 at.% Cu in the $Ti_{41}Zr_{25}Be_{34-x}Cu_x$ BMG system, Cu4 had the maximum value of hardness (7.27 GPa).

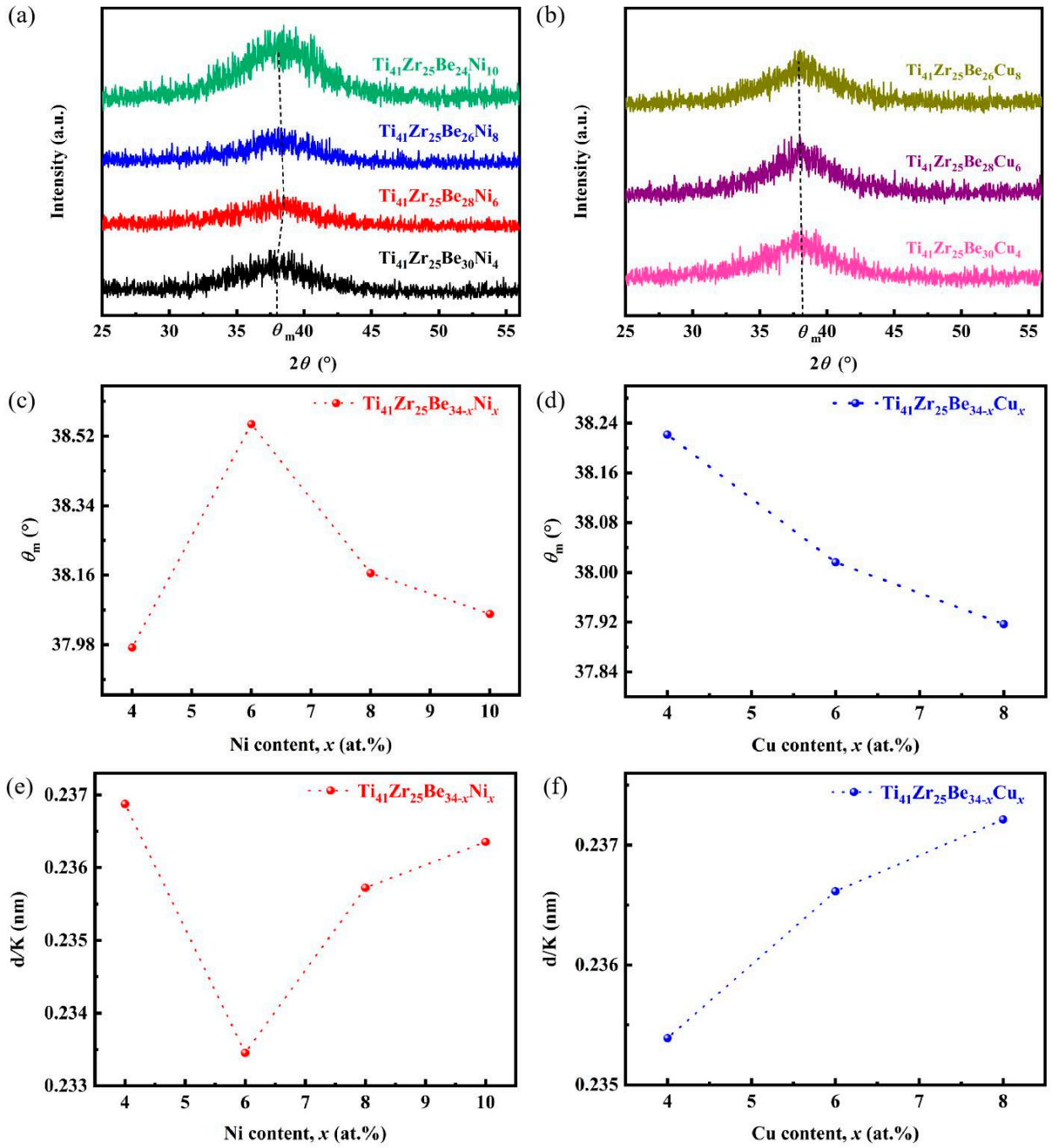

Figure 6. Relationship of θ_m and d/K with the change of chemical composition in $Ti_{41}Zr_{25}Be_{34-x}Ni_x$ BMGs and Cu content of $Ti_{41}Zr_{25}Be_{34-x}Cu_x$ BMG systems. (**a**) Magnified maximal diffracted intensity in XRD pattern of $Ti_{41}Zr_{25}Be_{34-x}Ni_x$ BMGs. (**b**) Magnified maximal diffracted intensity in XRD pattern of $Ti_{41}Zr_{25}Be_{34-x}Cu_x$ BMGs. (**c**) Change of θ_m as a function of Ni content for $Ti_{41}Zr_{25}Be_{34-x}Ni_x$ BMGs. (**d**). Change of θ_m as a function of Cu content for $Ti_{41}Zr_{25}Be_{34-x}Cu_x$ BMGs. (**e**) The correlation between the d/K and Ni content for $Ti_{41}Zr_{25}Be_{34-x}Ni_x$ BMGs. (**f**) The correlation between the d/K and Cu content for $Ti_{41}Zr_{25}Be_{34-x}Cu_x$ BMGs.

5. Conclusions

Two BMG systems of Ti-based $Ti_{41}Zr_{25}Be_{34-x}Ni_x$ and $Ti_{41}Zr_{25}Be_{34-x}Cu_x$ BMGs were prepared using a copper mold suction casting method and the effect of Ni and Cu content on the thermoplastic formability, viscosity, and nanoindentation was studied. The current work is summarized as follows:

1. The viscosity of Ti-based BMGs exhibited a gradual decrease of several orders of magnitude with increasing temperature in the SCLR, and the TPF is influenced by both the viscosity and the width of the SCLR. In $Ti_{41}Zr_{25}Be_{34-x}Ni_x$ BMGs, the TPF decreased with increasing Ni content, and $Ti_{41}Zr_{25}Be_{30}Ni_4$ exhibited the highest TPF compared with the other alloys due to its wider SCLR and lower values of viscosity in the SCLR. Conversely, for $Ti_{41}Zr_{25}Be_{34-x}Cu_x$ BMGs, the TPF was enhanced with increasing Cu content, reaching its peak at 8 at.% Cu ($Ti_{41}Zr_{25}Be_{26}Cu_8$). This result is similarly ascribed to its wider SCLR and lower viscosity in the SCLR.
2. The nanoindentation tests reveal that the hardness and modulus of $Ti_{41}Zr_{25}Be_{34-x}Ni_x$ BMGs exhibited an initial increase followed by a decrease with increasing Ni content. Specifically, at 6 at.% Ni, the highest values of hardness (7.26 GPa) and modulus (125.8 GPa) were observed. Furthermore, the hardness and modulus of $Ti_{41}Zr_{25}Be_{34-x}Cu_x$ decreased with increasing Cu content. At 4 at.% Cu, the alloy demonstrated the maximum values of hardness (7.27 GPa) and modulus (126.2 Gpa) among the $Ti_{41}Zr_{25}Be_{34-x}Cu_x$ BMGs. In this study, based on Bragg's law, the position of the maximal diffracted intensity θ_m was utilized to reflect the mean atomic distance, suggesting the variation in atomic density. This indicates the varying tendency of the hardness of Ti-based BMGs.

Author Contributions: Conceptualization, Y.C. and L.S.; Methodology, M.C., Y.H. and K.Y.; Validation, L.Z., W.L. and N.X.; Formal analysis, M.C.; Investigation, M.C.; Resources, L.S., N.X., Q.L., W.L. and J.W.; Data curation, M.C. and L.S.; Writing—original draft, M.C.; Writing—review & editing, L.S.; Visualization, M.C.; Supervision, L.Z., Q.L., J.W. and S.D.; Funding acquisition, L.Z., Y.C., S.D., Q.L., N.X., W.L., J.W. and L.S. All authors have read and agreed to the published version of the manuscript.

Funding: The authors would like to acknowledge the National Natural Science Foundation of China (No. 52201187), the Key R&D Program of Zhejiang (No. 2023C0082), the General Scientific Research Project of Zhejiang Provincial Education Department (No. Y202249336), and the Science and Technology Plan Project of Taizhou (Nos. 22gya18, 21gya23, 2002gy06).

Institutional Review Board Statement: Not applicable.

Informed Consent Statement: Not applicable.

Data Availability Statement: Data are contained within the article.

Conflicts of Interest: The authors declare no conflict of interest.

References

1. Wang, T.; Zhou, Y.; Zhang, L. Chemical and structural heterogeneity improve the plasticity of a Zr-based bulk metallic glass at low-temperature annealing. *J. Non-Cryst. Solids* **2023**, *603*, 122115. [CrossRef]
2. Ruschel, L.M.; Adam, B.; Gross, O.; Neuber, N.; Frey, M.; Wachter, H.-J.; Busch, R. Development and optimization of novel sulfur-containing Ti-based bulk metallic glasses and the correlation between primarily crystallizing phases, thermal stability and mechanical properties. *J. Alloys Compd.* **2023**, *960*, 170614. [CrossRef]
3. Shao, L.; Ketkaew, J.; Gong, P.; Zhao, S.; Sohn, S.; Bordeenithikasem, P.; Datye, A.; Mota, R.M.O.; Liu, N.; Kube, S.A.; et al. Effect of chemical composition on the fracture toughness of bulk metallic glasses. *Materialia* **2020**, *12*, 100828. [CrossRef]
4. Nomoto, K.; Ceguerra, A.V.; Gammer, C.; Li, B.; Bilal, H.; Hohenwarter, A.; Gludovatz, B.; Eckert, J.; Ringer, S.P.; Kruzic, J.J. Medium-range order dictates local hardness in bulk metallic glasses. *Mater. Today* **2021**, *44*, 48–57. [CrossRef]
5. Zhang, T.; Long, Z.; Peng, L.; Li, Z. Prediction of glass forming ability of bulk metallic glasses based on convolutional neural network. *J. Non-Cryst. Solids* **2022**, *595*, 121846. [CrossRef]
6. Deng, Y.; Wang, C.; Ding, F.; Zhang, T.; Wu, W. Thermo-mechanical coupled flow behavior evolution of Zr-based bulk metallic glass. *Intermetallics* **2023**, *152*, 107770. [CrossRef]
7. Li, N.; Pan, J.; Liu, Z.; Liu, L. Metallic glass nanostructures: Forming strategies and functional applications. *Mater. Today Adv.* **2022**, *15*, 100253. [CrossRef]
8. Zhang, M.; Wang, Y.; Ding, G.; Zheng, R.; Wei, R.; Zhang, G.; Sun, Q.; Zhao, X.; Liu, L. Biocompatible superhydrophobic surface on Zr-based bulk metallic glass: Fabrication, characterization, and biocompatibility investigations. *Ceram. Int.* **2023**, *49*, 25549–25562. [CrossRef]
9. Gu, J.; Shao, Y.; Shi, L.; Si, J.; Yao, K. Novel corrosion behaviours of the annealing and cryogenic thermal cycling treated Ti-based metallic glasses. *Intermetallics* **2019**, *110*, 106467. [CrossRef]

10. Du, P.; Xiang, T.; Cai, Z.; Xie, G. The influence of porous structure on the corrosion behavior and biocompatibility of bulk Ti-based metallic glass. *J. Alloys Compd.* **2022**, *906*, 164326. [CrossRef]
11. Tang, Y.L.; Zhang, T.W.; Shi, X.H.; Qiao, J.W.; Wang, Z.H.; Zhou, H.F.; Wu, Y.C. Design novel Ti-based metallic glass matrix composites with excellent dynamic plasticity. *J. Alloys Compd.* **2019**, *773*, 844–852. [CrossRef]
12. Li, H.F.; Zheng, Y.F. Recent advances in bulk metallic glasses for biomedical applications. *Acta Biomater.* **2016**, *36*, 1–20. [CrossRef] [PubMed]
13. Gu, J.-L.; Shao, Y.; Zhao, S.-F.; Lu, S.-Y.; Yang, G.-N.; Chen, S.-Q.; Yao, K.-F. Effects of Cu addition on the glass forming ability and corrosion resistance of Ti-Zr-Be-Ni alloys. *J. Alloys Compd.* **2017**, *725*, 573–579. [CrossRef]
14. Nishiyama, N.; Amiya, K.; Inoue, A. Novel applications of bulk metallic glass for industrial products. *J. Non-Cryst. Solids* **2007**, *353*, 3615–3621. [CrossRef]
15. Liens, A.; Etiemble, A.; Rivory, P.; Balvay, S.; Pelletier, J.-M.; Cardinal, S.; Fabrègue, D.; Kato, H.; Steyer, P.; Munhoz, T.; et al. On the Potential of Bulk Metallic Glasses for Dental Implantology: Case Study on $Ti_{40}Zr_{10}Cu_{36}Pd_{14}$. *Materials* **2018**, *11*, 249. [CrossRef] [PubMed]
16. Ma, X.; Li, Q.; Chang, L.; Chang, C.; Li, H.; Sun, Y. Enhancement on GFA and mechanical properties of Ni-based bulk metallic glasses through Fe addition. *Intermetallics* **2017**, *90*, 58–62. [CrossRef]
17. Men, H.; Pang, S.; Inoue, A.; Zhang, T. New Ti-Based Bulk Metallic Glasses with Significant Plasticity. *Mater. Trans.* **2005**, *46*, 2218–2220. [CrossRef]
18. Kai, W.; Kao, P.C.; Chen, W.S.; Lin, C.L.; Xiao, Z.H.; Hsu, C.F.; Lee, P.Y. The oxidation behavior of a $Ti_{50}Cu_{28}Ni_{15}Sn_7$ bulk metallic glass at 400–500 °C. *J. Alloys Compd.* **2010**, *504*, S180–S185. [CrossRef]
19. Wu, X.F.; Suo, Z.Y.; Si, Y.; Meng, L.K.; Qiu, K.Q. Bulk metallic glass formation in a ternary Ti–Cu–Ni alloy system. *J. Alloys Compd.* **2008**, *452*, 268–272. [CrossRef]
20. Zhang, X.F.; Kim, K.B.; Yi, S. Effects of Co on the microstructures and mechanical properties of $Ti_{50}Cu_{50-x}Co_x$ alloys (x = 0–25 at.%). *Philos. Mag. Lett.* **2010**, *90*, 43–50. [CrossRef]
21. Hao, G.J.; Lin, J.P.; Zhang, Y.; Chen, G.L.; Lu, Z.P. Ti–Zr–Be ternary bulk metallic glasses correlated with binary eutectic clusters. *Mater. Sci. Eng. A* **2010**, *527*, 6248–6250. [CrossRef]
22. Guo, F.; Wang, H.-J.; Poon, S.J.; Shiflet, G.J. Ductile titanium-based glassy alloy ingots. *Appl. Phys. Lett.* **2005**, *86*, 091907. [CrossRef]
23. Zhao, S.; Chen, N.; Gong, P.; Yao, K. Centimeter-Sized Quaternary Ti-Based Bulk Metallic Glasses with High Ti Content of 50 at%: Centimeter-Sized Quaternary Ti-Based Bulk Metallic. *Adv. Eng. Mater.* **2016**, *18*, 231–235. [CrossRef]
24. Zhao, S.F.; Shao, Y.; Gong, P.; Yao, K.F. A Centimeter-Sized Quaternary Ti-Zr-Be-Ag Bulk Metallic Glass. *Adv. Mater. Sci. Eng.* **2014**, *2014*, 192187. [CrossRef]
25. Zhao, S.F.; Gong, P.; Li, J.F.; Chen, N.; Yao, K.F. Quaternary Ti–Zr–Be–Ni bulk metallic glasses with large glass-forming ability. *Mater. Des.* **2015**, *85*, 564–573. [CrossRef]
26. Zhao, S.F.; Chen, N.; Gong, P.; Yao, K.F. New centimeter-sized quaternary Ti–Zr–Be–Cu bulk metallic glasses with large glass forming ability. *J. Alloys Compd.* **2015**, *647*, 533–538. [CrossRef]
27. Gong, P.; Li, F.; Jin, J. Preparation, Characterization, and Properties of Novel Ti-Zr-Be-Co Bulk Metallic Glasses. *Materials* **2020**, *13*, 223. [CrossRef] [PubMed]
28. Gong, P.; Wang, X.; Shao, Y.; Chen, N.; Yao, K. Ti-Zr-Be-Fe quaternary bulk metallic glasses designed by Fe alloying. *Sci. China Phys. Mech. Astron.* **2013**, *56*, 2090–2097. [CrossRef]
29. Tang, M.Q.; Zhang, H.F.; Zhu, Z.W.; Fu, H.M.; Wang, A.M.; Li, H.; Hu, Z.Q. TiZr-base Bulk Metallic Glass with over 50 mm in Diameter. *J. Mater. Sci. Technol.* **2010**, *26*, 481–486. [CrossRef]
30. Zhang, L.; Tang, M.Q.; Zhu, Z.W.; Fu, H.M.; Zhang, H.W.; Wang, A.M.; Li, H.; Zhang, H.F.; Hu, Z.Q. Compressive plastic metallic glasses with exceptional glass forming ability in the Ti–Zr–Cu–Fe–Be alloy system. *J. Alloys Compd.* **2015**, *638*, 349–355. [CrossRef]
31. Calin, M.; Gebert, A.; Ghinea, A.C.; Gostin, P.F.; Abdi, S.; Mickel, C.; Eckert, J. Designing biocompatible Ti-based metallic glasses for implant applications. *Mater. Sci. Eng. C* **2013**, *33*, 875–883. [CrossRef]
32. Zhang, C.; Ouyang, D.; Pauly, S.; Liu, L. 3D printing of bulk metallic glasses. *Mater. Sci. Eng. R Rep.* **2021**, *145*, 100625. [CrossRef]
33. Li, Z.; Huang, Z.; Sun, F.; Li, X.; Ma, J. Forming of metallic glasses: Mechanisms and processes. *Mater. Today Adv.* **2020**, *7*, 100077. [CrossRef]
34. Schroers, J. On the formability of bulk metallic glass in its supercooled liquid state. *Acta Mater.* **2008**, *56*, 471–478. [CrossRef]
35. Hasan, M.; Schroers, J.; Kumar, G. Functionalization of Metallic Glasses through Hierarchical Patterning. *Nano Lett.* **2015**, *15*, 963–968. [CrossRef]
36. Gong, P.; Kou, H.; Wang, S.; Deng, L.; Wang, X.; Jin, J. Research on thermoplastic formability and nanomoulding mechanism of lightweight Ti-based bulk metallic glasses. *J. Alloys Compd.* **2019**, *801*, 267–276. [CrossRef]
37. Cai, F.-F.; Sarac, B.; Chen, Z.; Czibula, C.; Spieckermann, F.; Eckert, J. Surmounting the thermal processing limits: Patterning TiZrCuPdSn bulk metallic glass even with nanocrystallization. *Mater. Today Adv.* **2022**, *16*, 100316. [CrossRef]
38. Cai, F.-F.; Blanquer, A.; Costa, M.B.; Schweiger, L.; Sarac, B.; Greer, A.L.; Schroers, J.; Teichert, C.; Nogués, C.; Spieckermann, F.; et al. Hierarchical Surface Pattern on Ni-Free Ti-Based Bulk Metallic Glass to Control Cell Interactions. *Small* **2023**. *early view*. [CrossRef]
39. Liu, Z.; Schroers, J. General nanomoulding with bulk metallic glasses. *Nanotechnology* **2015**, *26*, 145301. [CrossRef]

40. Bordeenithikasem, P.; Shen, Y.; Tsai, H.-L.; Hofmann, D.C. Enhanced mechanical properties of additively manufactured bulk metallic glasses produced through laser foil printing from continuous sheetmetal feedstock. *Addit. Manuf.* **2018**, *19*, 95–103. [CrossRef]
41. Pitt, E.B.; Kumar, G.; Schroers, J. Temperature dependence of the thermoplastic formability in bulk metallic glasses. *J. Appl. Phys.* **2011**, *110*, 043518. [CrossRef]
42. Schroers, J. Processing of Bulk Metallic Glass. *Adv. Mater.* **2010**, *22*, 1566–1597. [CrossRef] [PubMed]
43. Kawamura, Y.; Nakamura, T.; Inoue, A. Superplasticity in $Pd_{40}Ni_{40}P_{20}$ metallic glass. *Scr. Mater.* **1998**, *39*, 301–306. [CrossRef]
44. Zhang, W.; Tao, P.; Chen, Y.; Si, J.; Long, Z.; Huang, S.; He, H.; Huang, Z.; Yang, Y. Structural evolutionary behavior of Zr-based bulk metallic glasses under thermoplastic deformation. *Intermetallics* **2023**, *155*, 107831. [CrossRef]
45. Hu, Q.; Fu, M.W.; Zeng, X.R. Thermostability and thermoplastic formability of $(Zr_{65}Cu_{17.5}Ni_{10}A_{l7.5})_{100-x}RE_x$ (x = 0.25–3.25, RE: Y, Gd, Tb, Dy, Ho, Er, Tm, Yb, Lu) bulk metallic glasses. *Mater. Des.* **2014**, *64*, 301–306. [CrossRef]
46. Turnbull, D. Under What Cond. Can A Glass Be Form? *Contemp. Phys.* **1969**, *10*, 473–488. [CrossRef]
47. Lu, Z.P.; Liu, C.T. A new glass-forming ability criterion for bulk metallic glasses. *Acta Mater.* **2002**, *50*, 3501–3512. [CrossRef]
48. Kumar, G.; Tang, H.X.; Schroers, J. Nanomoulding with amorphous metals. *Nature* **2009**, *457*, 868–872. [CrossRef] [PubMed]
49. Zhang, W.; Miao, H.; Li, Y.; Chang, C.; Xie, G.; Jia, X. Glass-forming ability and thermoplastic formability of ferromagnetic $(Fe, Co, Ni)_{75}P_{10}C_{10}B_5$ metallic glasses. *J. Alloys Compd.* **2017**, *707*, 57–62. [CrossRef]
50. Parthiban, R.; Stoica, M.; Kaban, I.; Kumar, R.; Eckert, J. Viscosity and fragility of the supercooled liquids and melts from the Fe–Co–B–Si–Nb and Fe–Mo–P–C–B–Si glass-forming alloy systems. *Intermetallics* **2015**, *66*, 48–55. [CrossRef]
51. Stoica, M.; Ramasamy, P.; Kaban, I.; Scudino, S.; Nicoara, M.; Vaughan, G.B.M.; Wright, J.; Kumar, R.; Eckert, J. Structure evolution of soft magnetic $(Fe_{36}Co_{36}B_{19.2}Si_{4.8}Nb_{4)100-x}Cu$ (x= 0 and 0.5) bulk glassy alloys. *Acta Mater.* **2015**, *95*, 335–342. [CrossRef]
52. Pi, J.; Wang, Z.; He, X.; Bai, Y.; Zhen, R. Nanoindentation mechanical properties of glassy $Cu_{29}Zr_{32}Ti_{15}Al_5Ni_{19}$. *J. Alloys Compd.* **2016**, *657*, 726–732. [CrossRef]
53. Haag, F.; Beitelschmidt, D.; Eckert, J.; Durst, K. Influences of residual stresses on the serrated flow in bulk metallic glass under elastostatic four-point bending—A nanoindentation and atomic force microscopy study. *Acta Mater.* **2014**, *70*, 188–197. [CrossRef]
54. Schuh, C.A.; Nieh, T.G. A nanoindentation study of serrated flow in bulk metallic glasses. *Acta Mater.* **2003**, *51*, 87–99. [CrossRef]
55. Concustell, A.; Sort, J.; Alcalá, G.; Mato, S.; Gebert, A.; Eckert, J.; Baró, M.D. Plastic Deformation and Mechanical Softening of $Pd_{40}Cu_{30}Ni_{10}P_{20}$ Bulk Metallic Glass During Nanoindentation. *J. Mater. Res.* **2005**, *20*, 2719–2725. [CrossRef]
56. Oliver, W.C.; Pharr, G.M. An improved technique for determining hardness and elastic modulus using load and displacement sensing indentation experiments. *J. Mater. Res.* **1992**, *7*, 1564–1583. [CrossRef]
57. Borie, B. X-ray Diffraction in Crystals, Imperfect Crystals, and Amorphous Bodies. *J. Am. Chem. Soc.* **1965**, *87*, 140–141. [CrossRef]
58. Hufnagel, T.C.; Brennan, S. Short- and medium-range order in $(Zr_{70}Cu_{20}Ni_{10})_{90-x}Ta_xAl_{10}$ bulk amorphous alloys. *Phys. Rev. B* **2003**, *67*, 014203. [CrossRef]
59. Caron, A.; Wunderlich, R.; Louzguine-Luzgin, D.V.; Xie, G.; Inoue, A.; Fecht, H.-J. Influence of minor aluminum concentration changes in zirconium-based bulk metallic glasses on the elastic, anelastic, and plastic properties. *Acta Mater.* **2010**, *58*, 2004–2013. [CrossRef]
60. Bera, S.; Ramasamy, P.; Şopu, D.; Sarac, B.; Zálešák, J.; Gammer, C.; Stoica, M.; Calin, M.; Eckert, J. Tuning the glass forming ability and mechanical properties of Ti-based bulk metallic glasses by Ga additions. *J. Alloys Compd.* **2019**, *793*, 552–563. [CrossRef]
61. Yang, W.; Li, J.; Liu, H.; Dun, C.; Zhang, H.; Huo, J.; Xue, L.; Zhao, Y.; Shen, B.; Dou, L.; et al. Origin of abnormal glass transition behavior in metallic glasses. *Intermetallics* **2014**, *49*, 52–56. [CrossRef]
62. Sharma, S.; Suryanarayana, C. Effect of Nb on the glass-forming ability of mechanically alloyed Fe–Ni–Zr–B alloys. *Scr. Mater.* **2008**, *58*, 508–511. [CrossRef]
63. Lv, J.W.; Yin, D.W.; Wang, F.L.; Yang, Y.J.; Ma, M.Z.; Zhang, X.Y. Influence of sub-Tg annealing on microstructure and crystallization behavior of TiZr-based bulk metallic glass. *J. Non-Cryst. Solids* **2021**, *565*, 120855. [CrossRef]